Journal of The Electrochemical Society

The Electrochemical Society
Advancing solid state & electrochemical science & technology

Electrochemical and Degradation Studies on One-Dimensional Tunneled Sodium Zirconogallate (NZGO) + Yttria-Stabilized Zirconia (YSZ) Composite, Mixed Sodium and Oxygen Ion Conductor

To cite this article: Pooya Elahi *et al* 2022 *J. Electrochem. Soc.* **169** 114502

Journal of The Electrochemical Society, 2022 **169** 114502
1945-7111/2022/169(11)/114502/10/$40.00 © 2022 The Electrochemical Society (“ECS”). Published on behalf of ECS by IOP Publishing Limited

Electrochemical and Degradation Studies on One-Dimensional Tunneled Sodium Zirconogallate (NZGO) + Yttria-Stabilized Zirconia (YSZ) Composite, Mixed Sodium and Oxygen Ion Conductor

Pooya Elahi,[z] Jude Horsley, and Taylor D. Sparks[z]

Materials Science and Engineering Department, University of Utah, Utah 84112, United States of America

In recent years, multi-phase materials capable of multi-ion transport have emerged as attractive candidates for a variety of electrochemical devices. Here, we provide experimental results for fabricating a composite electrolyte made up of a one-dimensional fast sodium-ion conductor, sodium zirconogallate, and an oxygen-ion conductor, yttria-stabilized zirconia. The composite is synthesized through a vapor phase conversion mechanism, and the kinetics of this process are discussed in detail. The samples are characterized using diffraction, electron microscopy, and electrochemical impedance spectroscopy techniques. Samples with a finer grain structure exhibit higher kinetic rates due to larger three-phase boundaries (TPBs) per unit area. The total conductivity is fitted to an Arrhenius type equation with activation energies ranging from 0.23 eV at temperatures below 550 °C to 1.07 eV above 550 °C. The electrochemical performance of multi-phase multi-species, mixed Na^+ and O^{2-} conductor, is tested under both oxygen chemical potential gradient as well as sodium chemical potential gradient are discussed using the Goldman-Hodgkin-Kats (GHK) and the Nernst equation.

[DOI: 10.1149/1945-7111/ac9ee2]

Manuscript submitted June 11, 2022; revised manuscript received September 29, 2022. Published November 7, 2022.

There has been enormous research in ionic conducting materials that enable electrochemical devices. The vast majority of research has focused on single-phase materials capable of conducting a single ionic species.[1–9] Some single-phase materials, such as rare-Earth oxide doped perovskites, are capable of multi-species transport (e.g., $[H^+]$, $[O^{2-}]$, and $[e', h^\bullet]$).[10–12] However, it is not thermodynamically possible to tune the total conductivity of the single-phase with simultaneous transport of multiple charged species.[13] Recently, the third class of ionic conductors has emerged where a composite consisting of multiple phases is able to accomplish uncoupled simultaneous transport of multiple ionic species. For example, Na-β''-alumina + yttria-stabilized zirconia (YSZ),[14] Na-β''-alumina + samaria-doped ceria (SDC),[15] sodium zirconogallate+YSZ[16,17] and others[18] are notable examples of composite materials having uncoupled cation and anion transport (e.g., Na^+ and O^{2-}) occurring through two separate but contiguous phases. These composites could be utilized for other functions such as providing selective chemical species transport to inject or remove specific species from a gas stream or chemical reaction. Moreover, one could envision numerous composite systems with features such as an increased number of mobile species for enhanced electrochemical performance and ameliorated mechanical properties of brittle electrolytes, such as strengthening observed in $Na - B'' - Alumina + YSZ$.[19]

Sodium-ion storage devices have been considered the most promising candidate for large-scale energy storage systems owing to sodium abundancy in nature and the low price of the resources compared to other candidates such as lithium.[20] Hence, the development of high-performance sodium-ion devices for applications in energy storage devices, including sodium-ion batteries (SIBs),[21] sodium-sulfur batteries,[22] sodium-air batteries,[23] or sodium-ion hybrid capacitors[24] is of great importance to improve synthesis and electrochemical properties for highly efficient utilization of renewable energies. High one-dimensional sodium ion conductivity has been observed when a tetravalent ion like Zr^{4+} or Ti^{4+} occupied some of Ga^{3+} sites in sodium gallate, to form $Na_{0.7}Zr_{0.3}Ga_{4.7}O_8$ (hereafter NZGO) or $Na_{0.7}Ti_{0.3}Ga_{4.7}O_8$ (hereafter NTGO).[16,25,26] This fast sodium ion conductor contains one-dimensional tunnels (diameter ~2.5 Å) serving as pathways for sodium-ion transport in a monoclinic crystal system.[27,28] These channels are large enough to make the NZGO an excellent sodium ion conductor and additionally a good candidate for ion exchange for other monovalent cations such as K^+, Li^+, and Ag^+ possibly using molten salts. The channels lie parallel to the b-axis with continuous hexagonal cross-section and low activation energy ($E_a \approx 0.25$ eV) for sodium ions. Prior work on pure NZGO and NTGO noted limitations of these materials primarily due to the high energy cost of synthesis (>1600 °C for up to 48 h),[25] formation of a liquid phase,[29] the requirement for encapsulation of samples within platinum crucibles,[30] and low mechanical strength of the pure single-phase NZGO and NZTO. Our prior work[31] showed that the NZGO + YSZ composite could be successfully fabricated using Ga_2O_3 + YSZ mixture via a vapor phase process. The Electrochemical Impedance Spectroscopy (EIS) indicated the sodium- and oxygen-ion conductivity of the NZGO + YSZ. In this work, we attempt to study the effect of the microstructure of as-sintered Ga_2O_3 + YSZ samples on the vapor phase conversion kinetics, discussing the conversion mechanism and characterizing the converted NZGO + YSZ electrolyte by diffraction, microscopy, and spectroscopy techniques. The open-circuit voltage (OCV) of the cell fabricated using the NZGO + YSZ composite electrolyte corresponding to Goldman-Hodgkin-Katz potential was measured under oxygen and sodium chemical potential gradient and compared with the Nernst potential before and after reaching equilibrium time to show the effect of ion transient process in OCV measurements. Finally, the sample's degradation was studied after ~400 h of operation at 1190 °C.

Experimental Methods

Synthesis of pre-conversion sample.—Gallium oxide powder (Alfa Aesar) was calcined in a furnace at 720 °C in air for 2 h to ensure phase transformation of α-gallia to β-gallia. Then, β-gallia was mixed with 8YSZ powder (Tosoh) in a weight ratio of 7: 3, followed by wet milling in ethanol for 5 h at 300 rpm in a planetary ball mill (Fritsch Pulverisette) using yttria-stabilized zirconia media (MSE supplies). The slurry was collected and dried overnight at room temperature in air and dried in an oven at 100 °C (Fisher Scientific) for 10 h. The powder was sieved #70 (ASTME 11) and pelletized using a stainless-steel die and a uniaxial hydraulic press (Carver) at 110 MPa, followed by cold isostatic pressing (Autoclave Engineers) at 250 MPa. Pellets were sintered in air at 1300 °C, 1400 °C, 1500 °C, and 1600 °C for 3 h using a chamber furnace (Deltech). The density of as-sintered samples was measured using the gas pycnometry method (Anton Paar) in helium.

---

[z] E-mail: pooya.elahi@utah.edu; sparks@eng.utah.edu

Synthesis of packing powder.—Na-β''-alumina powder was used as a packing powder as the Na_2O vapor source. Due to the high cost of gallium oxide and low diffusivity of Ga^{3+} in Al_2O_3,[32] $Na-\beta''-$alumina was used as Na_2O gas source instead of $Na-\beta''-$gallia. Polycrystalline Na- β''-alumina was separately fabricated using the zeta process using Na_2CO_3 (Millipore Sigma), Li_2O (Millipore Sigma), and $\alpha-Al_2O_3$ (Baikowski) corresponding to ~8.85 wt% Na_2O, ~0.75 wt% Li_2O, and balance Al_2O_3, respectively, can be found elsewhere.[33]

Vapor-phase conversion and characterization.—The as-sintered pre-conversion pellets (Ga_2O_3 + YSZ) were loosely buried in the vapor phase packing powder ($Na\_\beta''-Al_2O_3$) in an alumina crucible covered with an alumina lid. The encapsulated as-sintered samples were placed in a muffle furnace (Across International) for 5 to 30 h with 5 h intervals at 1250 °C. According to the binary phase diagram of $Na_2O-Al_2O_3$ system,[34] the conversion temperature could be chosen in a reasonably broad range from ~1200 °C to ~1550 °C. In the current work, T = 1250 °C was selected as the conversion temperature, considering three reasons. First, to avoid any possibly liquid phase formation close to the eutectic reaction occurring around ~1550 °C. Second, to prevent phase transformation at ~1400 °C resulting in precipitation of intermediate sodium aluminate ($NaAlO_2$), which occurs mainly at the grain boundaries and deteriorates mechanical strength. Third, to optimize the kinetics and thermodynamics of the reactions to minimum loss of Na_2O from the packing powder and to lower the energy demand for the process. The conversion kinetics of the Ga_2O_3 + YSZ samples to NZGO + YSZ was characterized via X-ray diffraction using $Cu_{K\alpha} = 1.5406$ Å radiation (Bruker, D2 Phaser). Rietveld refinement was conducted using the full-pattern Rietveld method based on least-squares refinement using GSAS II[35] Samples were cross-sectioned using a high precision diamond saw (Allied High Tech) and fine polished to 200 nm (Buehler). After polishing, samples were thermally etched at 100 °C below sintering temperatures for 1 h. For SEM imaging (FEI Quanta 600 FEG), polished surfaces were 5 nm carbon coated (Gatan 682 PECS) to reduce the electron charging effect. The grain size was measured by the mean linear intercept method using ImageJ software.[36]

Electrochemical characterization.—Electrochemical characterization was carried out under two different scenarios. Open-Circuit Voltage (OCV) measurements were made under applied oxygen chemical potential gradient and sodium chemical potential gradient. In the first series of experiments, an oxygen chemical potential gradient was achieved by exposing one side of the sample to a reducing atmosphere consisting of oxygen, hydrogen and water vapor (where, $p_{H_2O}, p_{H_2} \gg p_{O_2}$) while the other side was exposed to air ($p_{O_2} \approx 0.21$ atm). In the second series, a sodium chemical potential gradient was achieved by fabricating two different electrodes with a variation of sodium chemical potential in two sets. The first set of experiments was conducted using Ga_2O_3 + Na- β''-gallia and β + β''-gallia where synthesis methods are described elsewhere[37] and the second set using Na- β/β''-alumina and Al_2O_3 + Na- β''-alumina. A fine Platinum gauze (Alfa Aesar) was placed over the screen-printed Pt paste (Heraeus) as current collectors on both sides of the fully converted sample (NZGO + YSZ) and the device was mechanically pressed together with screws. For all experiments, pristine NZGO + YSZ pellets were used. Diffusional mass transport in these devices needs to reach equilibrium. Therefore, the experiments were conducted before and after the necessary relaxing time to reach equilibrium. The time to reach the equilibrium, τ, is a function of sample thickness, l, and chemical diffusion coefficient of the mobile species, $\tilde{D}$, which according to Thangadurai and Weppner,[38] in the absence of the electrical field, can be estimated by

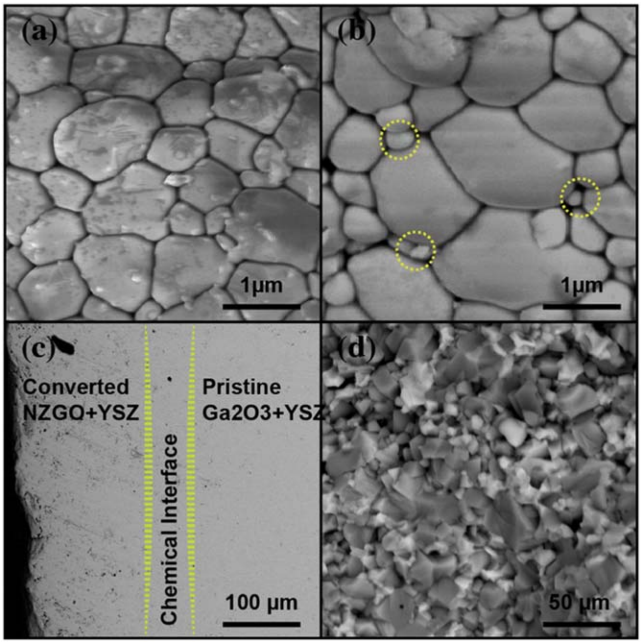

Figure 1. SEM micrograph of (a) the thermally etched $Ga_2O_3 + YSZ$ pellet as-sintered at 1400 °C, (b) at 1600 °C (newly formed fine grains noted with dashed circles), (c) partially converted specimen at 1250 °C after 5 h, and (d) fully converted *NZGO* + *YSZ*.

$$\tau = \frac{l^2}{\tilde{D}_i^{n\pm}}$$

The open-circuit voltage (OCV) was measured using a high impedance electrometer (Keithley 6514) having input impedance >200 TΩ for voltage measurements and also charge measurements down to 10 fC to avoid any current leakage and minimize the meter contribution to the sample resistance. The actual sample temperature was measured using a K-type thermocouple (Omega) and a precision multimeter (Keithley 2000) with 0.001 °C resolution. In each series of experiments, the samples were kept at 1000 °C for 100 h for possible degradation studies. Electrochemical Impedance Spectroscopy (EIS) (Solartron- Impedance/Gain-Phaser Analyzer SI 1260 & Electrochemical interface SI 1287) was performed on samples within a frequency range of 1 MHz to 1 Hz, with 10 mV amplitude from ~200 °C to ~800 °C. Energy Dispersive Spectroscopy (EDS) was utilized to analyze possible elemental changes adjacent to the electrodes after the test. Porous platinum electrodes (Heraeus) were screen printed symmetrically on both sides of the fully converted pellets (t ~ 10 μm) and fired at 950 °C for 45 min. The EIS analysis was carried out using the circuit model shown in Fig. 3. The inductive resistance and contribution of lead wires and testing setup were obtained by shorting the leads in the empty cell setup (without the sample) and subtracting this measurement from EIS data points. The obtained data were fitted to semicircles. The intercept of the extrapolation of the x-axis at the high-frequency regime was considered as the total sample resistance.

Result and Discussion

Figures 1a–1d shows the cross-sectional Scanning Electron Microscope (SEM) micrograph of the Ga_2O_3 + YSZ as-sintered at 1400 °C and 1600 °C, after thermal etching at 100 °C below sintering temperature for 1 h, partially converted sample after five hours of exposure to sodium oxide vapor and fabricated NZGO + YSZ sample after full conversion. Figures 1a and 1b represent the micrograph of the as-sintered Ga_2O_3 + YSZ at 1400 °C and 1600 °C. The microstructure of the sintered samples showed an

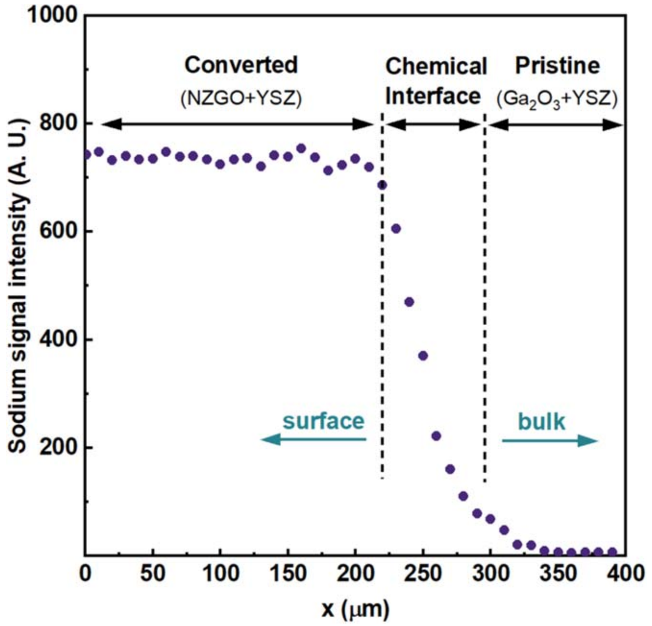

Figure 2. The EDS spectra of the linear scan for sodium contents across the sample's cross-section (x, distance from the surface) of the partially converted sample sintered at 1400 °C after exposure to the Na_2O vapor source at 1250 °C for 5 h.

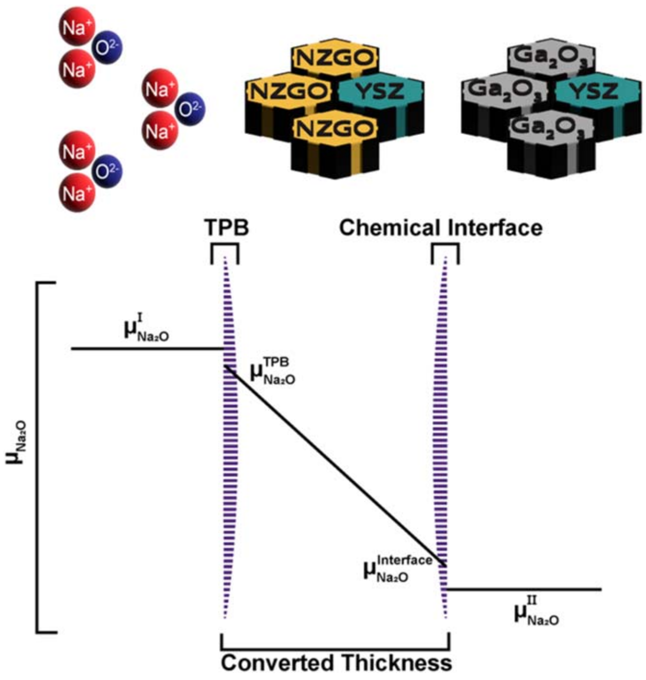

Figure 3. The schematic illustrated the Na_2O chemical potential gradient (μ_{Na_2O}) across the sample's thickness during the conversion process consists of one diffusive and two interfacial reactions.

increase in grain size as expected. However, newly formed fine grains were observed in the sample sintered at 1600 °C (dashed circles in Fig. 1b). These fine grains are formed due to the high sintering temperature with respect to the formation of the liquid phase in $Ga_2O_3 - Y_2O_3$ and $Ga_2O_3 - ZrO_2$ systems. Therefore, an uneven distribution of grains was observed, which will be discussed in detail in Fig. 5.

Figure 1c shows the SEM micrograph of the sample sintered at 1400 °C and partially converted at T = 1250 °C for 5 h. The converted thickness is measured to be ~220 μm after 5 h. The chemical interfacial band where the reaction Ga_2O_3NZGO happened is shown as well. The reaction front for the Ga_2O_3NZGO vapor phase conversion happened to be smoother and more uniform compared to previously published works on vapor phase conversion of Al_2O_3 to $Na - \beta'' -$ alumina using 20SDC[15] or 10Sc1CeZr[18] as oxygen-ion conductors which occurred to be sharper and highly porous. The sharp interface band with newly formed pores in the conversion of $\alpha - Al_2O_3$ to $Na - \beta'' -$ alumina occurred due to the large changes in the *c*-axis parameter of $\alpha\ - Al_2O_3$ to $Na - \beta'' -$ alumina unit cell causing significant structural volume change when $\alpha - Al_2O_3$ (corundum, c = 12.9 Å)[39] transform into $\beta'' -$ alumina (trigonal, c = 33.75 Å).[40] This large unit cell's volume change causes the formation of new pores and changes in the sample's density. However, in the conversion of $\beta - Ga_2O_3$ to NZGO both structures maintained monoclinic crystals with identical centrosymmetric space groups (C/2m) as well as alike lattice parameters (Ga_2O_3: a = 12.23 Å, b = 3.04 Å, c = 5.8 Å, β = 103.7°, NZGO: a = 12.38 Å, b = 3.015 Å, c = 9.14 Å, β = 122.28°).[41] Therefore, NZGO crystal structure is akin to Ga_2O_3, though different in the β angle of the unit cell, having a higher degree of uniformity at the interface, more minor volume change and less porosity in the converted sample.

Figure 2 represents the linear Energy-Dispersive X-ray Spectroscopy (EDS) spectra across the sample's cross-section of the partially converted sample at 1250 °C for 5 h. The higher intensity counts of the sodium content in converted thickness closer to the sample's surface indicates the chemical diffusion of the sodium species toward the sample bulk down the chemical potential gradient of the sodium (and sodium oxide) ($J^{TPB}_{Na} \propto -\nabla\mu_{Na}$ and $J^{Interface}_{Na_2O} \propto -\nabla\mu_{Na_2O}$) by incorporation of Na_2O vapor. The EDS spectra on the converted region showed an almost homogenous sodium content of ~740 counts with a decrease to ~600 at the chemical interface, while a dramatic decrease in sodium count to ~15 occurred at the other end of the chemical interfacial band where reaction front propagates by the coupled diffusion of Na^+ and O^{2-} ions toward the pristine region (Ga_2O_3 + YSZ).

The chemical potential gradient of the sodium oxide, as it is schematically demonstrated in Fig. 3, consists of two interfacial reactions at the three-phase boundaries (TPBs) and chemical interface and one diffusive reaction at the converted region. A chemical interfacial layer separated pristine and converted regions with a thickness of ~70 μm. Figure 3 shows the schematic of a one-dimensional model (along the *x*-axis) of the chemical potential gradient of sodium oxide species adjacent to the sample surface, the TPBs, the converted thickness, the reaction interface, and the pristine region. In this schematic, the $\mu^{I}_{Na_2O}$ and $\mu^{II}_{Na_2O}$ are the chemical potentials of the sodium oxide species in the Na_2O gaseous phase (vapor source) and the pristine (unconverted) region, respectively. The $\mu^{TPB}_{Na_2O}$ and $\mu^{Interface}_{Na_2O}$ are the sodium oxide chemical potentials adjacent to the TPBs and the reaction front adjacent to the pristine Ga_2O_3 + YSZ boundaries.

Figure 4 shows the densification behavior of the as-sintered Ga_2O_3 + YSZ converted NZGO + YSZ samples at 1200 °C to 1600 °C with 100 °C intervals, and grain size relationship to the sintering temperature. The data shows a maximum achieved density ($\rho_{rel\%}$ = 97.2%) at 1400 °C. The sample sintered at 1500 °C almost reached a similar density ($\rho_{rel\%}$ = 95.4%); however, the relative density of the sample sintered at 1600 °C unexpectedly decreased to 92% of relative density. Most sintered ceramics show a sigmoidal densification behavior where a plateau occurs after achieving high densities.[42–44] The expected sigmoidal fit to obtain density data (1200 °C to 1400 °C) without considering unexpected behaviors is shown in Fig. 4, in case the typical sintering behavior would be observed. However, some oxide systems deviate from this common

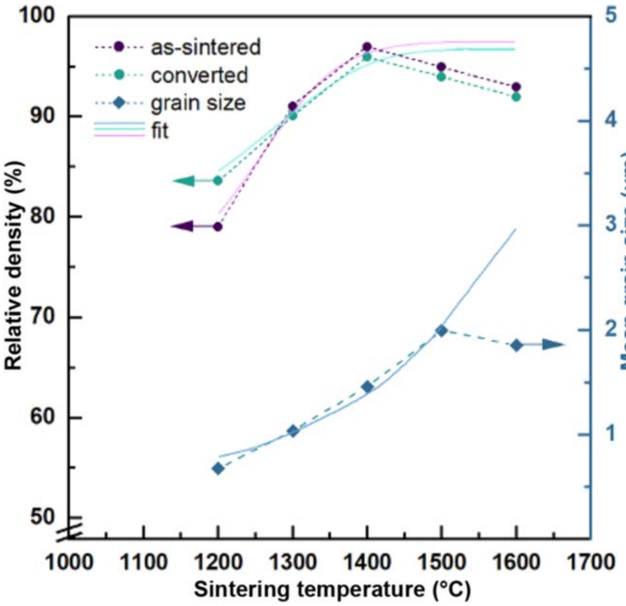

Figure 4. The relative density percentage of as-sintered and converted samples and the corresponding as-sintered samples' mean grain size (considering both phases $Ga_2O_3 + YSZ$) as a function of sintering temperatures.

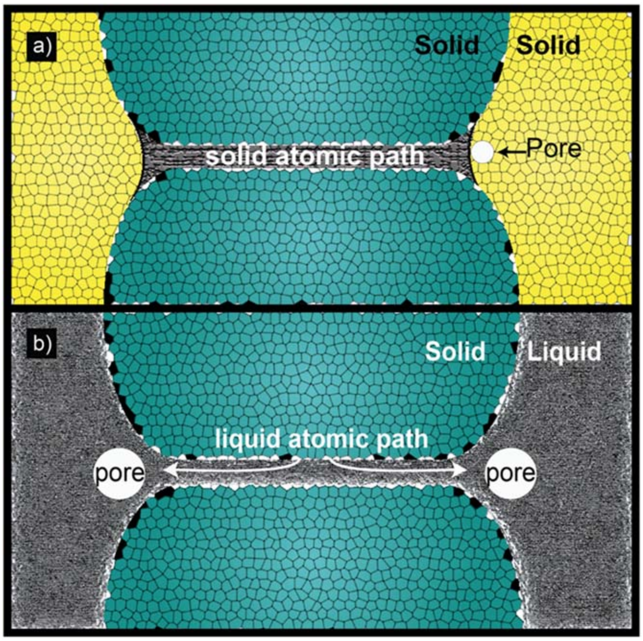

Figure 5. Sketch of the two-phase model comparing the microstructural aspect of (a) solid-state sintering at T < 1500 °C and (b) solid-liquid phase at $T > 1500$ °C.

trend, known as inadequate densification[43] due to full or partial surface melting in the high energy regions such as grain boundaries at temperatures close to the melting point of one of the components or possible phase transformation reactions such as eutectic reactions. In the binary systems of $Ga_2O_3 - Y_2O_3$,[45] and $Ga_2O_3 - ZrO_2$,[46] a heterogeneous microstructure consisting of both large and fine grains and also a reduction in density was unexpectedly observed for samples sintered at T > 1500 °C. The $\beta - Ga_2O_3$ has a much lower melting point than the other oxides in this study ($T_m^{Ga_2O_3} = 1725$ °C) [47] caused an undesired liquid phase during the solid-state sintering along with the presence of a eutectic reaction. The same densification behavior has also been studied in other systems such as $Ga_2O_3 - TiO_2$,[48] $Ga_2O_3 - La_2O_3$,[49] $Ga_2O_3 - Sm_2O_3$,[50] and $Ga_2O_3 - Gd_2O_3$.[50] Figure 5 schematically illustrates the inadequate densification in $Ga_2O_3 - Y_2O_3 - ZrO_2$ system.

The dissolution of air in newly melted regions at T > 1500 °C, additionally to the sub-grain formation while there was insufficient time for pores to pass the grain boundaries, caused inadequate densification. In such a system, the average grain size decreases close to the eutectic point due to an increase in the number of newly formed fine-grains, resulting in an increase in the total number of grains (considering grains in both phases) per unit area.[51] A solution to inadequate densification can be addressed by using pressure-assisted sintering or increasing the time and temperature of the process to thoroughly perform the liquid-phase sintering process, which was not the case for this study.

Figure 6 shows the average converted thickness of as-sintered Ga_2O_3 + YSZ to NZGO + YSZ via vapor phase process after 5 to 30 h of exposure to Na_2O vapor source. The samples sintered at 1400 °C which exhibited the highest achieved density in this study, showed a higher average converted thickness within the same exposure time. In Fig. 6, the obtained data of the current work were compared to the similar vapor phase conversion of a different system of alumina + 20SDC to $Na - \beta'' -$ alumina + 20SDC as mixed sodium and oxygen ion conductors[15] where the exact conversion mechanism happened using $Na - \beta'' -$ alumina as Na_2O vapor source. The conversion process consists of coupled diffusion of sodium and oxygen ions through sodium and oxygen ion conductors. The comparison of Al_2O_3 and Ga_2O_3 conversion process derived from the extensive structural similarities between gallia and alumina systems where most phases are analogous.[52]

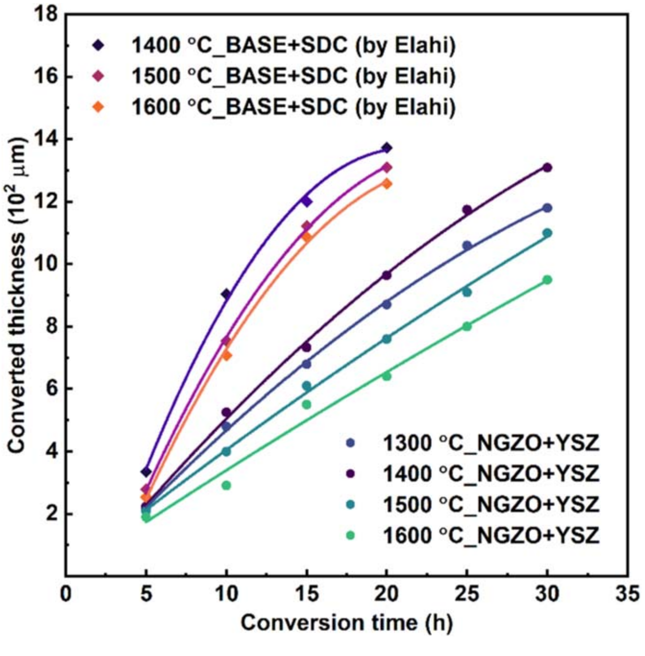

Figure 6. The conversion thickness versus conversion time of NZGO + YSZ in comparison to similar work done by Elahi et al.[15] on $Na - \beta'' -$ alumin. Both systems show a polynomial conversion behavior.

The samples with finer grains and higher densities show a faster kinetic rate and higher converted thickness than coarse-grain microstructures in both systems. This is consistent with previous theoretical and experimental works on vapor phase conversion of $Na - \beta'' -$ alumin + YSZ,[53] and $Na - \beta'' -$ alumin + SDC. Hence, fine-grained structures and a higher density of sintered samples facilitated the conversion of vapor phase. Parthasarathy and Virkar[53] suggested a general equation for such a conversion to

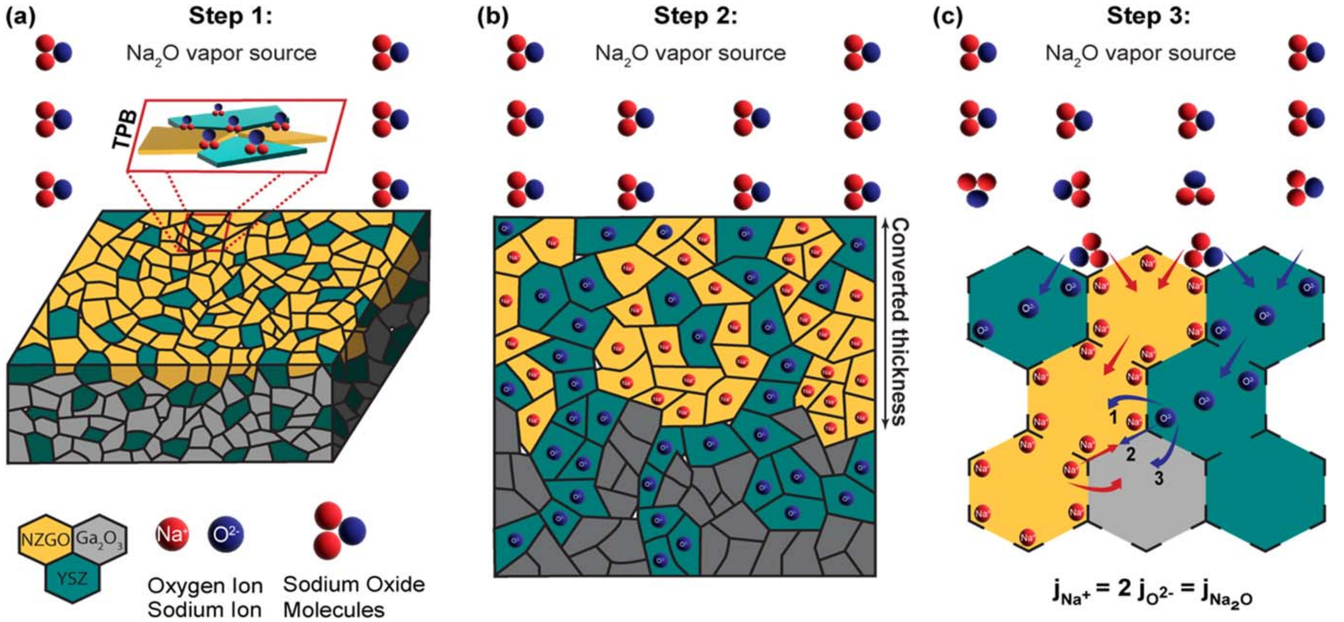

Figure 7. The schematic illustrates the reaction steps. (a) The pristine as-sintered $Ga_2O_3 + YSZ$ is exposed to the sodium oxide gas molecules. The reaction proceeds by the incorporation of Na_2O molecules and adsorption to the surface of the sample. Initially, a thin layer of *NZGO* will be formed on the surface and propagate at the TPBs (gas /*NZGO*/*YSZ*). (b) The conversion process continues by the coupled diffusion of Na^+ and O^{2-} ions through two contiguous networks of *NZGO* and *YSZ*, respectively. (c) At the third step, at the reaction interface, the oxygen ions (same for Na^+) can diffuse into *NZGO* (path 1), or transport along the $NZGO/Ga_2O_3/YSZ$ interface (path 2) or Ga_2O_3 (path 3).

predict the kinetics of the vapor phase conversion for two-phase materials

$$\frac{(x^2 - x_0^2)}{D_{eff}} + \frac{(x - x_0)}{K_{eff}} = t - t_0$$

where t is the required time to achieve the thermal equilibration, t_0 is incubation time which before no conversion happens, x_0 is initial converted thickness, D_{eff} is effective diffusion coefficient, K_{eff} is effective interface coefficient. In this study, the conversion time is considered as the dwell time once the conversion temperature is achieved (1250 °C). It is noteworthy that due to the high partial vapor pressure of Na_2O at temperatures below 1250 °C, there is an expected initial converted thickness at the surface on the order of a few microns at $T_{ramp} \leqslant T_{dwell} \approx 1250$ °C. Therefore, before reaching the conversion temperature, the extrapolation of the polynomial fit does not meet at zero but is slightly greater than zero ($x_0 > 0$ at $t = 0$). In some other cases, it is also possible that a negative extrapolation of polynomial fit for x_0 ($x_0 < 0$ at $t = 0$) occurs. Such a condition can be the case provided that some morphological changes at the surface occur (i.e., grain boundary grooving) prior to incorporation of Na_2O at the three-phase boundaries (TPB s). The polynomial fit of data points proves the conversion of Ga_2O_3 + YSZ happen to have a lower kinetic rate, although the extrapolation of the x-axis before reaching conversion temperature is almost in the same order of a few microns for both alumina and the gallia systems. The mathematical reason for the lower conversion rate is attributed to the lower mobility of the mobile species since $D^{NZGO}_{Na^+} < D^{\beta''}_{Na^+}$ and $D^{YSZ}_{O^{2-}} < D^{SDC}_{O^{2-}}$, therefore $D^{NZGO/YSZ}_{eff} < D^{\beta''/SDC}_{eff}$, also Na_2O flux (j_{Na_2O}) is a function of diffusivity of mobile species, then $j^{NZGO/YSZ}_{Na_2O} < j^{\beta''/SDC}_{Na_2O}$ resulted in $K^{NZGO/YSZ}_{eff} < K^{\beta''/SDC}_{eff}$ and lower slop of the fit. In other words, Na − β'' − alumina is a two-dimensional sodium-ion conductor compared to NZG O which is a one-dimensional Na^+ conductor, therefore, there will be less maneuverability for Na^+ ions within the structure. Besides, 20SDC has higher oxygen ionic conductivity compared to that of YSZ, which results in a lower conversion kinetic rate for NZGO + YSZ system.

The conversion mechanism of Ga_2O_3 + YSZ to NZGO + YSZ can be explained in three steps as illustrated in Figs. 7a–7c. In step 1, a thin layer of NZGO formed on the pellet's surface ($x_0 > 0$ at $t = 0$) (which initiated below reaching the conversion temperature 1250 °C) where Na_2O vapor partial pressure increased at ~600 °C − 700 °C in the covered crucible and Na_2O molecules are adsorbed to the solid surface as Na^+ and O^{2-} to form an initial NZGO layer in order of a few microns. At the TPBs, the following reaction happens:

$$Na_2O_{(TPB)} \rightarrow 2Na^+_{(NZGO)} + O^{2-}_{YSZ}$$

The TPBs length per unit area of the gas/solid interface is inversely proportional to the average grain diameter of both phases, $\bar{d}$. Therefore, a decrease in the average grain size ($\bar{d}$) results in a longer TPB and hence, a shorter diffusion distance and subsequently higher conversion thickness. Later, at sufficiently high temperatures (~800 °C − 900 °C), O^{2-} conduction is provided through the YSZ phase and Na^+ conduction takes place through the newly formed NZGO phase at the three-phase boundaries (TPBs) toward the interface between NZGO + YSZ and Ga_2O_3 + YSZ (step 2). In step 3, the incorporation of Na^+ and O^{2-} at the Ga_2O_3/NZGO/YSZ interface happens by the O^{2-} transport through possible paths 1, 2, and 3, where diffusion distance is estimated to be $\sim\frac{\bar{d}}{2}$. The overall chemical reaction for the synthesis of NZGO can be written as:

$$0.7\ Na^+_{NZGO} + 0.95\ O^{2-}_{YSZ} + 2.35\ Ga_2O_3 \rightarrow Na_{0.7}Zr_{0.3}Ga_{4.7}O_8$$

Since gallia is a refractory compound with a melting point of ~1725 °C, low vapor pressure at conversion temperature (1250 °C) was expected. Moreover, due to the low diffusivity of gallium ions in aluminum ions there isn't a considerable exchange of Ga^{3+} and Al^{3+}. Additionally, no evidence of diffusion of Y in NZGO or Ga in YSZ has been observed by the EDS in agreement with prior work.[31]

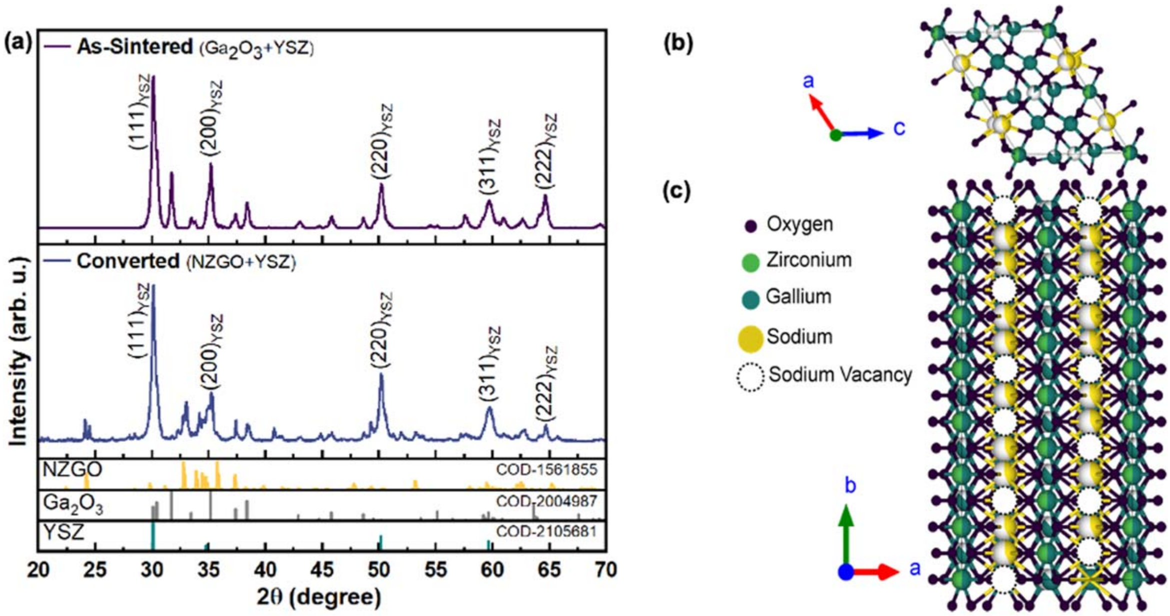

Figure 8. (a) XRD pattern of as-sintered $Ga_2O_3 + YSZ$ prior to conversion, and converted $NZGO + YSZ$, (b) schematic of $NZGO$ crystal structure parallel to b- and (c) c-axis.

Figure 8a shows the XRD pattern of the as-sintered Ga_2O_3 + YSZ pellet prior to conversion process and fully converted NZGO + YSZ. The Miller indices of the first five peaks of the YSZ phase are labeled. The measured lattice parameters of NZGO are $a = 12.38$ Å, $b = 3.015$ Å $c = 9.41$ Å, and $\beta = 122.28$ °, which is in a good agreement with previous works done on NZGO.[54] $Na_{0.7}Zr_{0.3}Ga_{4.7}O_8$ is identified One-dimension fast ion conductor with β –gallia –rutile intergroeth structure (BRG) when Ti^{4+} is replaced by Zr^{4+} (ionic radii of $Zr^{4+} = 72$ pm and $Ti^{4+} = 60$ pm [55]). Figures 8b and 8c show the NZGO unit cell perpendicular to the b- and c-axis. In $NZGO_{BGR}$, gallium resides in the edge-sharing octahedra and corner-sharing tetrahedra. Zirconium resides in the corner-sharing octahedra. Delocalized sodium ions reside in the hexagonal tunnels with a cross-section ~$2.5 - 3$ Å, where they can transport along b axis tunnels.

Galvanic measurements under oxygen and sodium chemical potential gradient.—In single-species ionic conductors, the Nernst equation can describe the cell potential. However, the Nernst equation is not valid for multi-species ionic conductor membranes. In this case, the cell potential for multi-species systems considering the transport properties of the migratory species can be calculated using the Godman-Hodgkin-Katz equation (aka GHK).[56–58] The GHK equation describes the cell potential in terms of transport parameters of permeates (here O^{2-}, Na^{+}, and electronic defects [e′]/[h˙]) and internal EMFs given in terms of chemical potentials of neutral species (μ_{O_2} and μ_{Na}). The GHK equation can be rewritten in terms of the chemical potential of neutral species at the electrodes, transport properties of the electrolyte and electrode polarization resistance which in other terms are individual Nernst voltages and transport parameters. Therefore, the cell potential (experimentally measured quantity) in terms of the different chemical potential of mobile species across the mixed sodium-ion (NZGO) and oxygen-ion (YSZ) conductor is given by:[13]

$$\mathrm{E_{cell}} = \left(\frac{\mathrm{E_{O_2}}}{\mathrm{ASR_{O^{2-}}}} + \frac{\mathrm{E_{Na}}}{\mathrm{ASR_{Na^+}}}\right) . \left[\frac{(\mathrm{ASR_{O^{2-}}}).(\mathrm{ASR_{Na^+}}).(\mathrm{ASR_e})}{[\mathrm{ASR_{O^{2-}}} . \mathrm{ASR_e}] + [\mathrm{ASR_{Na^+}} . \mathrm{ASR_e}] + [\mathrm{ASR_{O^{2-}}} . \mathrm{ASR_{Na^+}}]}\right]$$

where E_{O_2} and E_{Na} are Nernst potentials in volts corresponding to oxygen and sodium chemical potential respectively, $ASR_{O^{2-}}$, ASR_{Na^+} are the area specific resistance for oxygen, sodium ion transport, and ASR_e is the area specific electronic resistance in $\Omega.cm^2$. The cell area specific resistances are

$$\mathrm{ASR_{O^{2-}}} = \mathrm{r^c_{O^{2-}}} + \mathrm{r^{el}_{O^{2-}}} + \mathrm{r^a_{O^{2-}}}$$

$$\mathrm{ASR_{Na^+}} = \mathrm{r^c_{Na^+}} + \mathrm{r^{el}_{Na^+}} + \mathrm{r^a_{Na^+}}$$

$$\mathrm{ASR_e} = \mathrm{r^c_e} + \mathrm{r^{el}_e} + \mathrm{r^a_e}$$

where r^c_i is cathode/electrolyte interface electronic area specific resistance, ,r^a_i is anode/electrolyte interface electronic area specific resistance, r^{el}_i electrolyte electronic area specific resistance for oxygen-ion, sodium-ion and electronic defects in $\Omega.cm^2$, respectively. The total cell area specific resistance ($\Omega.cm^2$) is

$$\mathrm{ASR_{cell}} = \frac{(\mathrm{ASR_{O^{2-}}}).(\mathrm{ASR_{Na^+}}).(\mathrm{ASR_e})}{[\mathrm{ASR_{O^{2-}}} . \mathrm{ASR_e}] + [\mathrm{ASR_{Na^+}} . \mathrm{ASR_e}] + [\mathrm{ASR_{O^{2-}}} . \mathrm{ASR_{Na^+}}]}$$

and short circuit current density ($A.cm^{-2}$) is given by

$$\mathrm{I_{cell}} = \left(\frac{\mathrm{E_{O_2}}}{\mathrm{ASR_{O^{2-}}}} + \frac{\mathrm{E_{Na}}}{\mathrm{ASR_{Na^+}}}\right)$$

and the power density is the product of E_{cell} and I_{cell} in $W.cm^{-3}$.

Area specific resistance ASR for ion transfer across the membrane can be given in terms of fundamental charge transfer mechanisms and may be described by models such as the Butler-Volmer model.[13] For most solid-state membranes, area specific resistance (ASR) of the electronic defects is much greater than the ASR of permittable species. Note that the electron transport through the electrolyte is negligible, however, based on the local equilibrium assumption, electronic transport cannot mathematically be zero. The GHK equation defines the cell potential for multi-species conductors in terms of the individual Nernst voltages and transport parameters. For thin membranes, the interface effect dominant the transport properties (i.e., $r^c_{O^{2-}}$, $r^a_{O^{2-}}$, $r^c_{Na^+}$, and $r^a_{Na^+}$), however, provided that the membrane is not thin, the interface effect can be neglected. In the current work, the samples were fabricated in order of hundreds of microns therefore the ASR of the mobile species (permeates) are only function of electrolyte electronic specific area resistance ($r^{el}_{Na^+}$, $r^{el}_{O^{2-}}$ r^{el}_{e}). Therefore, generally under load current (I_L) when on both sides of the membrane $\nabla\mu_{Na} \cong 0$, the electrolyte is predominantly an O^{2-} ionic conductor where GHK equation reduces to $E^{measured}_{cell} = \varphi^{I} - \varphi^{II} = E_{O^2} - (I_L.ASR_{O^{2-}})$, which is consistence with only one species ionic conductor descriptions such as pure YSZ electrolyte in solid oxide fuel cell (SOFC).[59] When on both sides of the membrane $\nabla\mu_{O_2} \cong 0$, the electrolyte is a predominantly sodium-ion conductor, and $E^{measured}_{cell} = \varphi^{I} - \varphi^{II} = E_{Na} - (I_L.ASR_{Na^+})$ which is consistence with only one species ionic conductor descriptions such as pure NZGO electrolyte.

Figure 9 shows the measured open-circuit voltage (OCV) when the load current is zero ($I_L = 0$) before and after equilibration. That is when the load resistance is infinite (here $R_L > 200$ TΩ). In the first set of experiments, OCV was measured under applied oxygen chemical potential and was compared to the corresponding calculated Nernst voltage (E_{O^2}). When the concentration of sodium at anode and cathode is zero, the GHK potential results in theoretical Nernst potential. The Nernst potential (V or mV) can be calculated by

$$E_{O^2} = \frac{RT}{ZF} \ln \frac{p_{O^2_{out}}}{p_{O^2_{in}}}$$

where R is gas constant ($J.K^{-1}.mol^{-1}$), T is the absolute temperature (K), Z is the valence of the ionic species, F is the Faraday's constant ($C.mol^{-1}$), and p is oxygen partial pressure in air and fuel. Under the fuel cell mode (Fig. 9), both electrodes are reversible for oxygen and serve as source/sink for oxygen ions while they are blocking sodium ions since none of them contain any sodium; therefore, there is no sodium source. The lower measured voltage before and after reaching equilibration is attributed to the transient transport process of sodium ions before reaching equilibrium measured before time τ. Before time τ, due to the oxygen ion transport, the cathode is positively charged, and due to the electroneutrality to compensate for the generated voltage across the cell, sodium ions start to migrate (via diffusion mechanism) in the opposite direction from the anode to right to neutralize the induced voltage. The time required for diffusion of Na^+ ions, is τ. Therefore, by facilitating the Na^+ diffusion either by an increase in time or temperature, eventually, the transport of sodium ions ceased when the sodium ion electrochemical potential gradient approached zero, and both sets of data converged. However, after time τ, the measured voltage using a high impedance meter with negligible current flow through the meter and blocking electrodes to sodium ions, corresponds to the calculated Nernst voltage. The cell acts as a charged parallel plate capacitor after reaching equilibrium. While the capacitor impedance is inversely proportional to frequency, the capacitance doesn't contribute to the impedance measurement.

Figure 10 shows the cell voltage under applied sodium chemical potential gradient. In this study, two different electrodes were fabricated and used as the sodium source. The first set of electrodes were $\alpha-$alumina $+$ Na $-\beta$ $-$alumina and Na $-$ $\beta\&\beta''$ $-$ alumina electrodes, and the second set was measured using Ga_2O_3 + NZGO and NZGO + Na $-$ β'' $-$ gallia. During the OCV measurement of the cell, the oxygen partial pressure remained constant on both sides of the membrane at $p_{air} = 0.21$ atm. The sodium ions migrate down the chemical potential gradient, $j_{Na} \propto \nabla\mu_{Na}$. Therefore, by the migration of sodium ions from higher chemical potential to lower chemical potential, the electrode becomes positive. In the first set, the Na $-$ $\beta\&\beta''$ $-$ alumina electrode has a higher chemical potential of sodium, μ_{Na}, compared to that of $-$alumina + Na $-$ β $-$ alumina. Therefore, a sodium chemical potential gradient is established on both sides of the cell as the driving force of sodium ion transport. The OCV measurements were carried out from ~150 °C to 1200 °C, with 100 °C intervals. To represent the data, the polarity of the meter

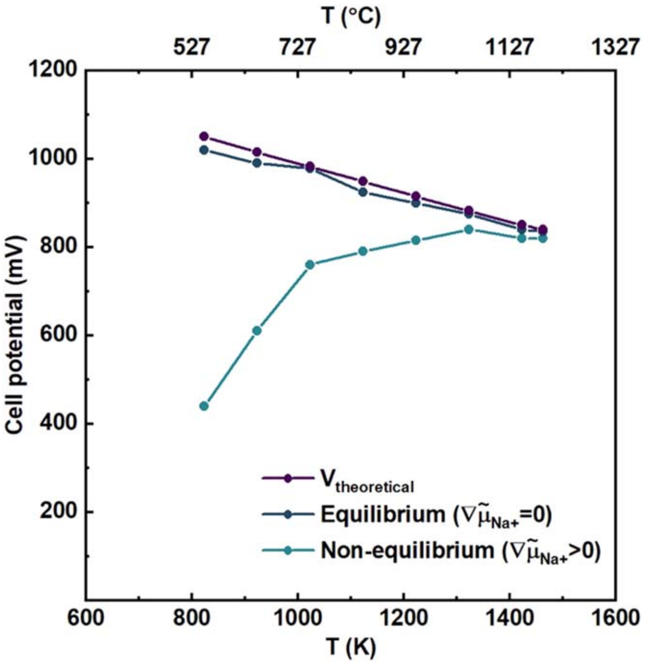

Figure 9. The Nernst potential (theoretical voltage) and the measured OCV of the fabricated cell under oxygen chemical potential gradient before and after the time τ to reach the equilibrium. The effect of the second mobile species (*Na*$^+$) is observed by reducing total cell voltage by a transient process to balance the generated potential due to the oxygen transport.

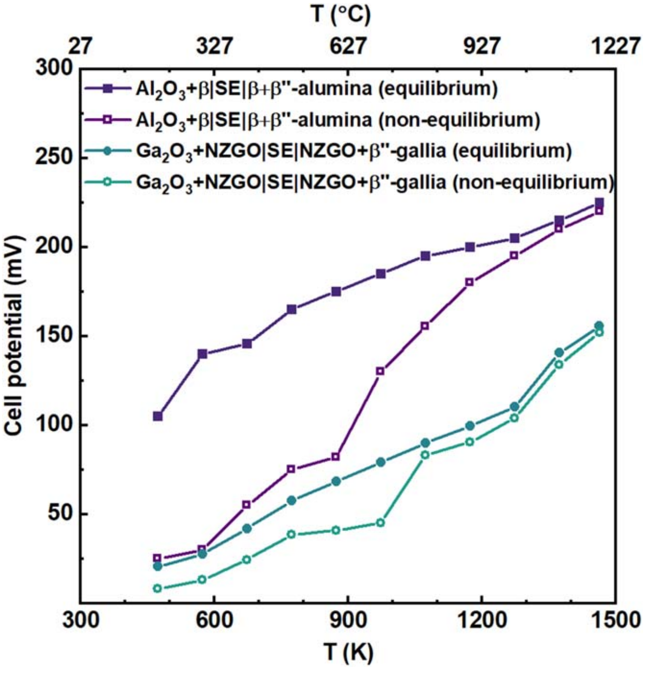

Figure 10. The measured cell potential under applied sodium chemical potential gradient provided by two different sets of electrodes, before and after time τ to reach equilibrium. The first set of data was obtained using α $-$alumina+Na$-\beta$ $-$alumina and $Na - \beta\&\beta'' - alumina$ electrodes, and the second set was obtained using $Ga_2O_3 + NZGO$ and $NZGO + Na - \beta'' - gallia$ electrodes.

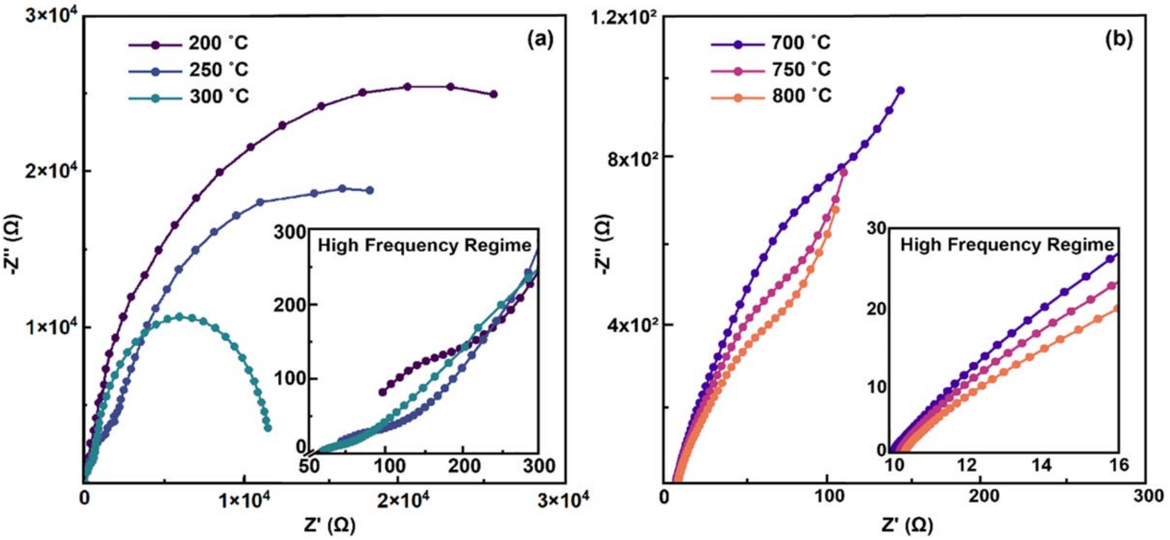

Figure 11. EIS spectra of the pristine converted samples in (a) low-temperature regime with the inset of the high-frequency regime and (b) high-temperature regimes with the inset of the high-frequency range.

was switched for positive voltage values. After time τ, the equilibrium is achieved, then cell voltage is given by

$$E_{Na} = \frac{RT}{ZF} \ln \frac{a^{L}_{Na}}{a^{R}_{Na}}$$

where $a^{R/L}_{Na}$ is the thermodynamic activity of sodium at the right or left electrode. The authors of this work couldn't find the values for the activity of Na in NZGO. However, the ratio of the activity in similar $Na - \beta -$ alumina has been reported to be 1 to 3.[60] The literature values of sodium activity in oxides, sulfides, or fluorites have exhibited high uncertainties due to the uncertainties in values of standard Gibb's free energy of formation (ΔG_f).[61]

Figures 11a to 11b shows Electrochemical Impedance Spectroscopy (EIS) spectra of the converted samples after full conversion. The data was obtained from 1 MHz to 1 Hz. Figure 11a corresponds to the high-frequency regime in the low-temperature regime (200 °C to 300 °C), and Fig. 11b shows EIS spectra corresponds to the high-frequency regime in the high-temperature regime (700 °C to 800 °C) temperatures. The EIS conditions such as electrode material, sintering temperature, sample thickness, and testing environment were constant for all samples. It has been proven that a significant effect resulting from inductive load from the leads and instrument contributes to the EIS data, especially at a high-frequency regime. Therefore, it is crucial to subtract the inductive load effect from the obtained data to eliminate the effect of instrumentation and leads.[62] This inductance appears as an imaginary part of the impedance data in the positive direction of the imaginary part of the impedance axis. Notably, there is a non-considerable dependence of inductance on temperature, unlike the sample's behavior. The extrapolation of the data to the x-axis (Z' real part of complex impedance) was considered as measured resistance. The equivalent circuit for the NZGO + YSZ sample is presented in Fig. 12a. In the high-frequency regime, grain boundary capacitances are shorted. Also, the electrode parameters (R^E, C^E) are not reflected in the high-frequency regime. Therefore, after subtraction of induction load from the data, at high-frequency intercepts, measured resistance can be given by

$$R^{\text{high freq.}}_{\text{total}} = \frac{R^{g}_{NZGO}\, R^{g}_{YSZ}}{R^{g}_{NZGO} + R^{g}_{YSZ}}$$

NZGO and YSZ both are well-known ionic conductors. At lower temperatures $R^{g}_{NZGO} < R^{g}_{YSZ}$ and at higher temperatures $R^{g}_{NZGO} > R^{g}_{YSZ}$. Thus, two main regimes were observed in the total conductivity plot, as shown in Fig. 12.

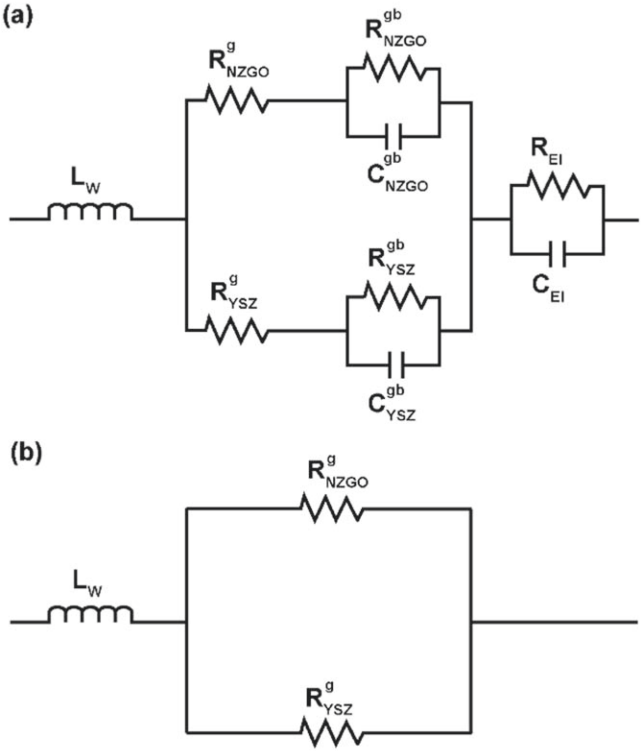

Figure 12. (a) The equivalent circuit for EIS analysis of multi-phase multi-species *NZGO + YSZ* ionic conductor. At high frequencies, the equivalent circuit will be simplified to (b) due to the shortening of grain boundaries capacitance and elimination of electrode polarization.

Figure 13a shows the Arrhenius plot of the total conductivity. The data points were fit to the conductivity equation

$$\sigma = \left(\frac{\sigma_0}{T}\right) \exp\left(-\frac{E_a}{k_B T}\right)$$

where σ_0 is the pre-exponential factor in S.cm^{-1}.K, T is the temperature in K, E_a is the activation energy, and κ_B is the

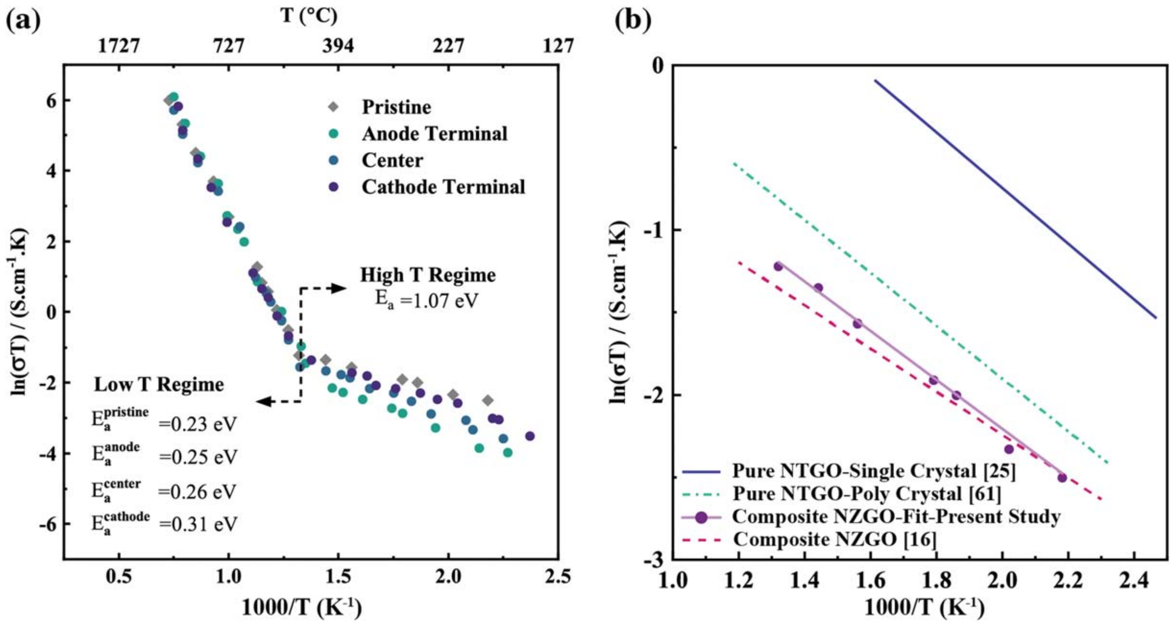

Figure 13. (a) The Arrhenius plot of the total conductivity of the sectioned cathode and anode vicinity of the degraded samples after running under experimental conditions for 396 h, compared with the center section and a pristine NZGO + YSZ sample with the corresponding calculated activation energies at low- and high-temperature regimes. (b) comparison of the present study in low-temperature regime with respect to single crystal NTGO,[25] polycrystal NTGO,[28] and polycrystal NZGO + YSZ.[16]

Boltzmann constant. The values of activation energy and pre-exponential factor have been obtained from the linear fits to the data presented in Fig. 13 and calculated to be $E_a^{pristine} = 0.23$ eV in the low-temperature regime for composite NZGO + YSZ and $E_a = 1.07$ eV for YSZ in high-temperature regime. The total conductivity of the degraded sectioned anode, cathode, and centerpiece of the sample was compared to the data obtained from a pristine sample. The total conductivity of the degraded sample slightly decreased in the low-temperature regime ($T < 550$ °C), where conductivity is mainly provided by sodium ions/vacancies ($R^g_{NZGO} < R^g_{YSZ}$). Regarding the degraded sample, the measured conductivity of the centerpiece showed values between the degraded cathode and anode terminals which is attributed to the slight sodium content concentration gradient from cathode to anode. The cathode terminal showed higher conductivity with respect to the anode terminal. Due to the high thermodynamic activity and high chemical potential of sodium, some sodium contents volatilized and caused a decrease in total conductivity. However, the mass transport of the Na^+ through the sample thickness from anode to cathode could be the reason for lower measured conductivity in low-temperature regime at anode compared to cathode terminal. In the high-temperature regime ($T > 550$ °C), where oxygen ion conductivity is dominant, $R^g_{NZGO} > R^g_{YSZ}$, all specimens exhibit almost identical conduction behavior, which attributed to the chemical and thermal refractory nature of the YSZ content. Figure 13b shows the low-temperature regime corresponding to the pure sodium conductivity. Data are compared with single crystal and polycrystal NTGO as well as composite polycrystal NZGO. NTGO and NZGO exhibit similar crystal structure. They only differentiate when Zr4 + substitute Ti4 + sites to form NZGO. As expected, composite ionic conductors exhibit properties in between pure components. The ionic conductivity of the NZGO measured to be lower than NTGO. Moreover, considerably lower than single crystal NTGO and NZGO (parallel to b-axis).

Conclusions

Composite multi-species ionic conductor electrolytes are envisioned as the next generation of solid electrolytes for optimum electrochemical and mechanical performance. Multi-phase multi-species sodium- and oxygen-ion conductor was fabricated using a vapor phase conversion process starting from an initial mixture of Ga_2O_3 + YSZ. The sintered pellets were exposed to a sodium oxide vapor source (using $Na - \beta -$ alumina) while encapsulated at 1250 °C. The samples converted to a sodium zirconogallate ($Na_{0.7}Zr_{0.3}Ga_{4.7}O_8$) and YSZ composite in about 10 h for a sample with 500 μm thickness. The process occurred via coupled diffusion of Na^+ ions through NZGO sodium-ion conductor and O^{2-} ions through YSZ. The crystal structure of the fabricated composite was investigated by XRD, SEM/EDS, and EIS techniques. The fabricated samples were studied under galvanic conditions applying oxygen chemical potential gradient and sodium chemical potential gradient. The data was compared to the Nernst voltage under each species' gradient. The NZGO + YSZ successfully showed both sodium- and oxygen-ion conduction. The tested samples were investigated for possible degradation under applied chemical potential gradients in low and high-temperature regimes. The degraded anode terminal showed lower conductivity than that of cathode and pristine samples, which was attributed to uneven distribution of sodium content through the sample bulk and loss of sodium contents in NZGO. However, in the high-temperature regime, conductivity remained unaltered, attributed to the refractory nature of YSZ under testing conditions.

Acknowledgments

This work was supported by the National Science Foundation under grant no. OMA-1936383 and DMR-1950589.

ORCID

Pooya Elahi https://orcid.org/0000-0002-8509-7096
Taylor D. Sparks https://orcid.org/0000-0001-8020-7711

References

1. J. B. Goodenough, "Oxide-ion electrolytes." *Annu. Rev. Mater. Res.*, **33**, 91 (2003).
2. S. (Rob) Hui, J. Roller, S. Yick, X. Zhang, C. Decès-Petit, Y. Xie, R. Maric, and D. Ghosh, "A brief review of the ionic conductivity enhancement for selected oxide electrolytes." *J. Power Sources*, **172**, 493 (2007).
3. X. J. Chen, K. A. Khor, S. H. Chan, and L. G. Yu, "Influence of microstructure on the ionic conductivity of yttria-stabilized zirconia electrolyte." *Mater. Sci. Eng. A*, **335**, 246 (2002).

4. B. G. Herman, K. Klier, G. W. Simmons, B. P. Finn, J. B. Bulko, T. P. Kobylinski, J. Catal, S. Jae Hong, K. Mehta, and A. V. Virkar, “Effect of microstructure and composition on ionic conductivity of rare-earth oxide-doped ceria.” *Electrochemical Society*, **145**, 638 (1998).
5. S. Anirban and A. Dutta, “Revisiting ionic conductivity of rare earth doped ceria: dependency on different factors.” *Int. J. Hydrogen Energy*, **45**, 25139 (2020).
6. N. M. Sammes, G. A. Tompsett, H. Näfe, and F. Aldinger, “Bismuth based oxide electrolytes— structure and ionic conductivity.” *J. Eur. Ceram. Soc.*, **19**, 1801 (1999).
7. Q. M. Nguyen and T. Takahashi, “Science and technology of ceramic fuel cells.” 366, https://scholar.google.com/scholar?hl=en&as_sdt=0%2C45&q=Science+and+Technology+of+Ceramic+Fuel+Cells&btnG= (1995).
8. V. V. Kharton, F. M. B. Marques, and A. Atkinson, “Transport properties of solid oxide electrolyte ceramics: a brief review.” *Solid State Ionics*, **174**, 135 (2004).
9. P. Elahi, E. Winterholler, and T. D. Sparks, “Effect of sintering conditions on the microstructure and electrochemical properties of 6scandia 1Ceria co-doped zirconia (6Sc1CeZr).” (2022).
10. A. A. Plazaola, A. Cruellas Labella, Y. Liu, N. B. Porras, D. A. Pacheco Tanaka, M. Van, S. Annaland, and F. Gallucci, “Mixed ionic-electronic conducting membranes (miec) for their application in membrane reactors: a review.” *Processes*, **7**, 128 (2019).
11. M. Papac, V. Stevanović, A. Zakutayev, and R. OHayre, “Triple ionic–electronic conducting oxides for next-generation electrochemical devices.” *Nat. Mater.*, **20**, 301 (2021).
12. A. V. Virkar, “(Invited) multi-species electrochemical transport through multi-phase materials.” *ECS Meet. Abstr.*, **MA2017-02**, 1685 (2017).
13. A. V. Virkar, “Transport through mixed proton, oxygen ion and electron (hole) conductors: Goldman–Hodgkin–Katz-type equation.” *J. Power Sources*, **194**, 753 (2009).
14. P. Parthasarathy and A. V. Virkar, “Vapor phase conversion of α-alumina + zirconia composites into sodium ion conducting Na-β'' -Alumina + Zirconia solid electrolytes.” *J. Electrochem. Soc.*, **160**, A2268 (2013).
15. P. Elahi, J. A. Horsley, and T. D. Sparks, “ECSarXiv preprints |¬¬synthesis and electrochemical study of multi-phase.” *Multi-Species Ion Conductor Sodium β''-Alumina (BASE) + 20SDC Using a Vapor-Phase Process* (2022), (https://ecsarxiv.org/7scvq/) (accessed June 5, 2022).
16. L. Ghadbeigi, Z. Liu, T. D. Sparks, and A. V. Virkar, “Synthesis of ion conducting sodium zirconium gallate + yttria-stabilized zirconia by a vapor phase process.” *J. Electrochem. Soc.*, **163**, A1560 (2016).
17. P. Elahi and A. V. Virkar, “Electrochemical studies on mixed Na + – O_2– ions conducting sodium zirconium gallate + YSZ composite.” *44th Int. Conf. Expo. Adv. Ceram. Compos., The American Ceramic Society, Daytona Beach, Florida* (https://ceramics.org/wp-content/uploads/2018/09/ICACC20_Abstracts_WebFinal.pdf) p. 58 (2020).
18. P. Elahi and T. D. Sparks, “Synthesis and electrochemical performance of multi-species.” *Multi-Phase BASE + 10Sc1CeZr as a Simultaneous Sodium and Oxygen Ion Conductor*, “(n.d.).”
19. S. C. Ligon, G. Blugan, M. C. Bay, C. Battaglia, M. V. F. Heinz, and T. Graule, “Performance analysis of Na-β''-Al2O3/YSZ solid electrolytes produced by conventional sintering and by vapor conversion of α-Al2O3/YSZ.” *Solid State Ionics*, **345**, 115169 (2020).
20. J. W. Fergus, “Ion transport in sodium ion conducting solid electrolytes.” *Solid State Ionics*, **227**, 102 (2012).
21. S. Song, H. M. Duong, A. M. Korsunsky, N. Hu, L. Lu, and A. Na , “Superionic conductor for room-temperature sodium batteries open.” *Nat. Publ. Gr.*, **6**, 32330 (2016).
22. T. Oshima, M. Kajita, and A. Okuno, “Development of sodium-sulfur batteries.” *Int. J. Appl. Ceram. Technol.*, **1**, 269 (2004).
23. P. Adelhelm, P. Hartmann, C. L. Bender, M. Busche, C. Eufinger, and J. Janek, “From lithium to sodium: Cell chemistry of room temperature sodium-air and sodium-sulfur batteries.” *Beilstein J. Nanotechnol.*, **6**, 1016 (2015).
24. Y. Yuan, C. Wang, K. Lei, H. Li, F. Li, and J. Chen, “Sodium-ion hybrid capacitor of high power and energy density.” *ACS Cent. Sci.*, **4**, 1261 (2018).
25. G. V. Chandrashekhar, S. C. Bandis, A. C. Lumsden, and N. R. Barton, “Important copyright information.” *Int. J. Rock Mech. Min. Sci. Geomech. Abstr.*, **20**, 249 (1983).
26. C. Li-chuan, A. Rabenau, and W. Weppner, “One-dimensional ionic conduction in solid Ag2 Tl6I10.” *Appl. Phys.*, **17**, 233 (1978).
27. Y. Onoda, Y. Michiue, M. Watanabe, S. Yoshikado, and T. Ohachi, “NMR study of one-dimensional ionic conductor, sodium titano-gallates (I).” *Solid State Ionics*, **79**, 45 (1995).
28. D. D. Edwards, N. H. Empie, N. Meethong, and J. W. Amoroso, “Synthesis and transport studies of one-dimensional ion conductors: AxGa4 + XTi1-xO8 (A = Li, Na, K).” *Solid State Ionics*, **177**, 1897 (2006).
29. D. D. Edwards, N. H. Empie, N. Meethong, and J. W. Amoroso, “Synthesis and transport studies of one-dimensional ion conductors: AxGa4 + XTi1−xO8 (A = Li, Na, K).” *Solid State Ionics*, **177**, 1897 (2006).
30. R. Hasegawa, M. Okabe, T. Asaka, N. Ishizawa, and K. Fukuda, “Structure and ionic conductivity of well-aligned polycrystalline sodium titanogallate grown by reactive diffusion.” *J. Solid State Chem.*, **229**, 252 (2015).
31. L. Ghadbeigi, Z. Liu, T. D. Sparks, and A. V. Virkar, “Synthesis of ion conducting sodium zirconium gallate + yttria-stabilized zirconia by a vapor phase process.” *J. Electrochem. Soc.*, **163**, A1560 (2016).
32. V. Apostolopoulos, L. M. B. Hickey, D. A. Sager, and J. S. Wilkinson, “Diffusion of gallium in sapphire.” *J. Eur. Ceram. Soc.*, **26**, 2695 (2006).
33. M. L. Miller, B. J. McEntire, G. R. Miller, and R. S. Gordon, “Prepilot process for the fabrication of polycrystalline BETA’-alumina electrolyte tubing.” *Am. Ceram. Soc. Bull.; (United States).*, **58**, 5 (1979).
34. C. W. Bale, P. Chartrand, S. A. Degterov, G. Eriksson, K. Hack, R. Ben Mahfoud, J. Melançon, A. D. Pelton, and S. Petersen, “Fact sage thermochemical software and databases.” *Calphad Comput. Coupling Phase Diagrams Thermochem.*, **26**, 189 (2002).
35. B. H. Toby and R. B. V. Dreele, “GSAS-II: the genesis of a modern open-source all purpose crystallography software package.” *Urn*, **46**, 544 (2013).
36. C. A. Schneider, W. S. Rasband, and K. W. Eliceiri, “NIH Image to IMAGEJ: 25 years of image analysis.” *Nat. Methods*, **9**, 671 (2012).
37. C. K. Kuo and P. S. Nicholson, “The formation of Na-β''-gallate in the $Na_2O{\cdot}Ga_2O_3$-Ga_2O_3 system.” *Solid State Ionics*, **118**, 251 (1999).
38. V. Thangadurai and W. Weppner, “Ce0.8Sm0.2O1.9: characterization of electronic charge carriers and application in limiting current oxygen sensors.” *Electrochim. Acta*, **49**, 1577 (2004).
39. M. Lucht, M. Lerche, H. C. Wille, Y. V. Shvyd’Ko, H. D. Rüter, E. Gerdau, and P. Becker, “Precise measurement of the lattice parameters of α-Al_2O_3 in the temperature range 4.5-250 K using the Mössbauer wavelength standard.” *J. Appl. Crystallogr.*, **36**, 1075 (2003).
40. M.-C. Bay, M. V. F. Heinz, A. N. Danilewsky, C. Battaglia, and U. F. Vogt, “Analysis of c-lattice parameters to evaluate Na_2O loss from and Na_2O content in ÃŽÂ^{2}’-alumina ceramics.” *Ceram. Int.*, **47**, 13402 (2021).
41. S. Geller, “Crystal structure of beta;-Ga_2O_3.” *J. Chem. Phys.*, **33**, 676 (1960).
42. G. W. SCHERER, “Sintering of low-density glasses: I.” *Theory, J. Am. Ceram. Soc.*, **60**, 236 (1977).
43. M. N. Rahaman, “Ceramic processing and sintering.” *Ceram. Process. Sintering* (CRC Press, New York, NY) 2nd ed.1 (2017), https://scholar.google.com/scholar?hl=en&as_sdt=0%2C45&q=Ceramic+processing+and+sintering&btnG=.
44. J. K. Mackenzie and R. Shuttleworth, “A phenomenological theory of sintering.” *Proc. Phys. Soc. Sect. B.*, **62**, 833 (1949).
45. V. F. Popova, A. G. Petrosyan, E. A. Tugova, D. P. Romanov, and V. V. Gusarov, “Y_2O_3-Ga_2O_3 phase diagram.” *Russ. J. Inorg. Chem.*, **54**, 624 (2009).
46. C. Barad, G. Kimmel, H. Hayun, D. Shamir, M. Shandalov, G. Shekel, and Y. Gelbstein, “Influence of galia (Ga_2O_3) addition on the phase transformations and crystal growth behavior of zirconia (ZrO_2).” *J. Mater. Sci.*, **53**, 12741 (2018).
47. P. Patnaik, “M.-H. New York Chicago san francisco lisbon london madrid mexico city milan new delhi san juan seoul, handbook of inorganic.” *Chemicals*, (2003).
48. S. Kamiya and R. J. D. Tilley, “Phase relations in the pseudobinary system $TiO_2-Ga_2O_3$.” *J. Solid State Chem.*, **22**, 205 (1977).
49. M. Zinkevich, S. Geupel, F. Aldinger, A. Durygin, S. K. Saxena, M. Yang, and Z. K. Liu, “Phase diagram and thermodynamics of the La_2O_3-Ga_2O_3.” *system revisited, J. Phys. Chem. Solids.*, **67**, 1901 (2006).
50. J. Nicolas, J. Coutures, J. P. Coutures, and B. Boudot, “Sm_2O_3 Ga_2O_3 and $Gd_2O_3-Ga_2O_3$ phase diagrams.” *J. Solid State Chem.*, **52**, 101 (1984).
51. G. P. Souza, P. F. Messer, and W. E. Lee, “Effect of varying quartz particle size and firing atmosphere on densification of brazilian clay-based stoneware.” *J. Am. Ceram. Soc.*, **89**, 1993 (2006).
52. L. M. Foster, G. V. Chandrashekhar, J. E. Scardefield, and R. B. Bradford, “Phase diagram of the system $Na_2O{\cdot}Ga_2O_3$-Ga_2O_3 and its relation to the system $Na_2O{\cdot}Al_2O_3$-Al_2O_3.” *J. Am. Ceram. Soc.*, **63**, 509 (1980).
53. P. Parthasarathy and A. V. Virkar, “Vapor phase conversion of α-alumina + zirconia composites into sodium ion conducting Na-β'' -alumina + zirconia solid electrolytes.” *J. Electrochem. Soc.*, **160**, A2268 (2013).
54. L. Ghadbeigi, Z. Liu, T. D. Sparks, and A. V. Virkar, “Synthesis of ion conducting sodium zirconium gallate + yttria-stabilized zirconia by a vapor phase process.” *J. Electrochem. Soc.*, **163**, A1560 (2016).
55. R. D. Shannon, “IUCr, Revised effective ionic radii and systematic studies of interatomic distances in halides and chalcogenides.” *Urn.*, **32**, 751 (1976).
56. T. F. Weiss, “Cellular Biophysics.” *Transport. A Bradford Book* (MIT Press, Cambridge) 1 (1996), https://scholar.google.com/scholar?hl=en&as_sdt=0%2C45&q=Cellular+Biophysics%2C+Volume+1%3A+Transport&btnG=.
57. D. Junge, *Nerve and muscle excitation* (1992).
58. P. J. Gellings, *Handbook of Solid State Electrochemistry* (CRC press, New York, NY) (2019), https://scholar.google.com/scholar?q=Gellings%C2%A0P.+J.,+Handbook+of+Solid+State+Electrochemistry+(CRC+press)+(2019&hl=en&as_sdt=0&as_vis=1&oi=scholart.
59. S. C. Singhal and K. Kendall, “High-temperature solid oxide fuel cells: fundamentals, design, and applicatons.” *Elsevier Advan. Techno.*, 405, https://scholar.google.com/scholar?hl=en&as_sdt=0%2C45&q=High-temperature+solid+oxide+fuel+cells%E2%80%AF%3A+fundamentals%2C+design%2C+and+applicatons&btnG= (2003).
60. M. Itoh and Z. Kozuka, “Measurement of Na2O activity in beta-alumina by EMF method.” *Transactions of the Japan institute of metals*, **26**, 353 (1985).
61. J. Liu and W. Weppner, “Beta″-alumina solid electrolytes for solid state electrochemical CO_2 gas sensors.” *Solid State Commun.*, **76**, 311 (1990).
62. L. Zhang, F. Liu, K. Brinkman, K. L. Reifsnider, and A. V. Virkar, “A study of gadolinia-doped ceria electrolyte by electrochemical impedance spectroscopy.” *J. Power Sources*, **247**, 947 (2014).